Geoscience Frontiers 14 (2023) 101617

HOSTED BY

Contents lists available at ScienceDirect

Geoscience Frontiers

journal homepage: www.elsevier.com/locate/gsf

Research Paper

# How high can fracture porosity become in the ultra-deep subsurface?

Jin Lai [a,b,*], Fei Zhao [b], Mei Zhang [b], Tianyu Bai [b], Yuyue Huang [b], Dong Li [b], Guiwen Wang [a,b], Ziqiang Qin [c]

[a] State Key Laboratory of Petroleum Resources and Prospecting, China University of Petroleum (Beijing), Beijing 102249, China
[b] College of Geosciences, China University of Petroleum (Beijing), 102249, China
[c] Department of Petroleum Engineering, University of Wyoming, Laramie, WY 82071, USA

ARTICLE INFO

*Article history:*
Received 27 October 2022
Revised 7 March 2023
Accepted 10 April 2023
Available online 15 April 2023
Handling Editor: R.D. Nance

*Keywords:*
Fracture porosity
Image log
Ultra-deep
In-situ stress
Dissolution

ABSTRACT

Knowledge of how high can fracture porosity become in the ultra-deep burial conditions is important but remains problematic. Fracture aperture and porosity are measured using X-ray computed tomography (CT) at atmospheric pressure and then calculated by image logs. Special attention is paid to how high fracture porosity can become in ultra-deep (>6000 m) settings, and which situations will result in high fracture porosities. In situ stress magnitudes, which can be calculated using well logs, control fracture performances, and dissolution along fracture improve fracture porosity at ultra-deep burial depths. Low horizontal stress difference ($\Delta\sigma$ < 25 MPa), very high fracture density will result in a high fracture porosity. Fracture porosity can keep as high as 2.0% in relatively low in situ stress conditions even at ultra-deep burial depths. In intense in situ stress conditions ($\Delta\sigma$ > 45 MPa), a high degree of dissolution along the fracture dramatically increases fracture porosity. Dissolution will result in the vuggy fracture planes and improve fracture porosity up to 2.0%. The results provide insights into the detection, characterization, and modeling of subsurface fractures.



## 1. Introduction

Fracture patterns and attributes, which govern fluid flow and rock strength, have long been a challenging topic in the Earth sciences (Lai et al., 2018; Laubach et al., 2019; Hyman et al., 2021; Shen et al., 2022). Fracture provides hydrocarbon and $CO_2$ storage spaces, and constitutes the main fluid flow conduits, and therefore has an important effect on reservoir behavior and performance (Nelson, 2001; Zeng et al., 2013; Zeng et al., 2013; Laubach et al., 2019; Lai et al., 2022a; Zhang et al., 2022). Therefore, the detection (recognition of fractured zones) and characterization (understanding fracture properties including fracture aperture and porosity) of subsurface natural fractures are important (Prioul et al., 2007; Tokhmchi et al., 2010; Movahed et al., 2014; Lai et al., 2018; Pengda et al., 2022). However, subsurface fractures are difficult to detect, and the multi-scale properties of fractures are notoriously challenging to characterize, quantify, and model (Laubach et al., 2019; Spooner et al., 2021; Lai et al., 2022b). Image logs (electrical and acoustic) provide an image of the borehole, and are particularly useful in fracture detection and evaluation where continuous drill cores are unavailable (Massiot et al., 2017; Lai et al., 2021; Lai et al., 2023a).

The presence of fractures can improve permeability by 1–2 orders of magnitude, however, fracture porosity is generally <0.5%, especially in low-permeability sandstone reservoirs (Zeng and Liu, 2010). In addition, in the ultra-deep burial conditions, fracture porosity will be further reduced due to overburden stress (Lai et al., 2017). Therefore, understanding fracture properties in the ultra-deep subsurface is very important (Tokhmchi et al., 2010; Zazoun, 2013; Lai et al., 2018). However, little study has been performed on how high can fracture porosity become in the ultra-deep subsurface. In this study, natural fractures are evaluated and quantitively analyzed using core, thin sections, and CT analysis, and then the fracture properties (aperture and porosity) are calculated. Then fractured zones are detected by electrical image logs, and the fracture porosity and aperture are characterized by electrical image logs to unravel how high the fracture porosity can reach in ultra-deep burial depths. In situ stress magnitudes play important roles in controlling fracture behaviors. Low $SH_{max}$ and $Sh_{min}$ difference (<25 MPa), and high fracture density (>2 numbers of fracture per meter) will result in a high fracture porosity (>2.0%). Additionally, in the intense in situ stress conditions, a high degree of dissolution along fracture surfaces will increases fracture porosity.

* Corresponding author at: China University of Petroleum-Beijing, 18 Fuxue Road, Changping, Beijing 102249, China.
*E-mail address:* laijin@cup.edu.cn (J. Lai).

https://doi.org/10.1016/j.gsf.2023.101617

## 2. Samples and methods

### 2.1. Core observation and analysis

Drilled core samples were taken from deep to ultra-deep depth intervals (4500–8100 m), and the core surfaces were 360° scanned to describe lithology, sedimentary structures as well as natural fractures (Fig. 1). Thin sections were prepared from core plugs (cut into 30 μm thickness), and were impregnated with blue epifluorescent epoxy to highlight porosity and micro-fractures (Fig. 2). Special aims were paid on the different carbonate cement generations filling in the fractures using a Cathode Luminescence (CL) optical microscope (Fig. 2). The laser scanning confocal microscope (LSCM), in which the light source is a laser but not standard mercury arc lamp, was also used for imaging fracture and pore spaces in the microscopic scales (Chandra and Vishal, 2021; Fig. 2).

The fracture aperture for each fracture surface and fracture porosity were calculated using two-dimensional (2-D) slice analysis and three-dimensional (3-D) visualization and counting of CT analysis (Lai et al., 2017; Fig. 3). The fracture surface area and volume can be calculated by 3-D visualization counting, and fracture porosity of each core is calculated by dividing the total fracture volume by the volume of the core segment. In addition, the fracture aperture is determined by dividing the total fracture volume by the scanned area (Lai et al., 2017; Fig. 3).

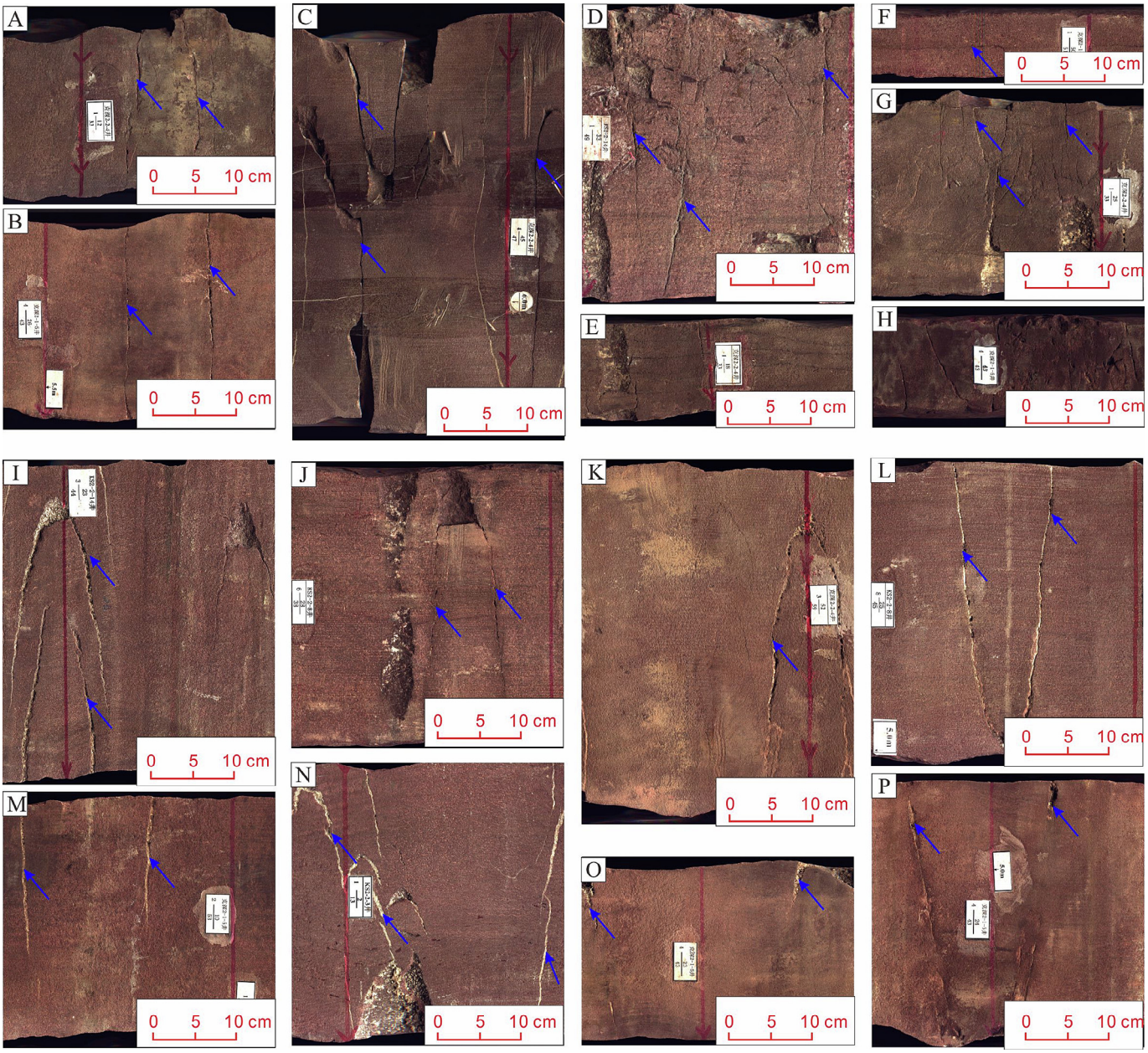


**Fig. 1.** Core photos showing the fractures in Cretaceous Bashijiqike Formation of Kuqa depression of Tarim Basin. (A) Open vertical fracture, KS 2-2-4. (B) Open vertical fracture, KS 2-1-5. (C) Open high angle fracture, KS 2-2-4. (D) Open network (horizontal, high angle and vertical) fracture, KS 2-2-4. (E) Open horizontal fracture, KS 2-2-4. (F) Open horizontal fracture, KS 2-1-5. (G) Open network (horizontal, high angle and vertical) fracture, KS 2-2-4;. (H) Partly cemented high angle and nearly vertical fracture, KS 2-2-14. (I) Partly cemented high angle fracture, KS 2-2-14. (J) Partly cemented high angle fracture, KS. (K) Partly cemented high angle fracture, KS 2-2-8. (L) Cemented vertical fracture, KS 2-1-5. (M) Calcite cemented high angle fracture, KS 2-2-3. (N). Calcite cemented high angle fracture and late stage dissolution, KS 2-1-5. (O) Calcite cemented high angle fracture and late stage dissolution, KS 2-1-5. (P) Dissolution and calcite cementation along fracture surface, KS 2-1-5.

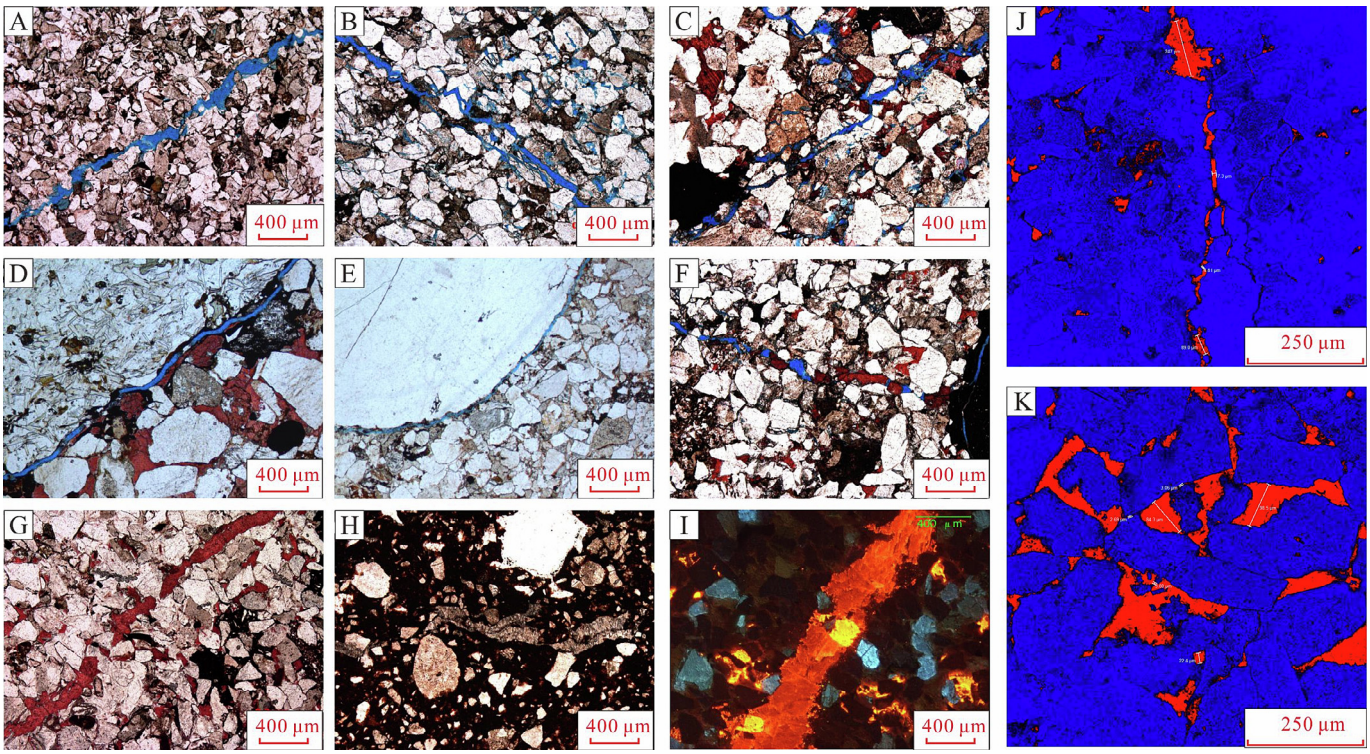


**Fig. 2.** Microscopic images revealing the fracture aperture in Cretaceous Bashijiqike Formation of Kuqa depression of Tarim Basin. (A) Microfracture and related framework grain dissolution, KS 242, 6568.95 m, $K_1bs$. (B)Microfracture and enlargement by dissolution, Dabei 9, 4854.2 m, $K_1bs$. (C) Microfracture crosscutting the framework grains, Dabei 9, 4853.1 m, $K_1bs$. (D) Microfracture around the grain boundary, Bozi 21, 6399.56 m $K_1$bx. (E) Grain boundary microfracture, Bozi 21, 6398.76 m, $K_1bx$. (F) Microfracture partly filled by calcite cements, Dabei 9, 4853.75 m, $K_1bs$. (G) Microfracture fully cemented by calcite cements, KS 242, 6567.51 m, $K_1bs$. (H) Microfracture fully cemented by dolomite cements, Bozi 12, 7003.75 m, $K_1bx$. (I) Carbonate cemented fractures, Dabei 12, 5399.26 m. (J) Microfracture, Dabei 12, 5440.19 m. (K) Intergranular pores and interganular dissolution pores, Dabei 12, 5451.41 m.

Fracture porosity using CT at atmospheric pressure are different from those calculated by image logs (Lai et al., 2017).

### 2.2. Image logs

Image logs measure the electrical resistivity or acoustic impedance around the borehole, and the raw data can be converted into a high resolution (up to 5 mm) "pseudo-picture" of the borehole wall through speed correction, eccentering correction and normalization (Prioul et al., 2007; Khoshbakht et al., 2009; Massiot et al., 2015; Lai et al., 2018). Then structural and sedimentological features (fracture, fault, bedding), which appear as sinusoidal waves, can be manually picked out from the image logs (Donselaar and Schmidt, 2005; Wilson et al., 2013; Brekke et al., 2017; Lai et al., 2022b). In addition, the sinusoidal waves of the dynamically normalized image logs can be used for the determination of dip direction and angle. The amplitude of sinusoidal waves indicates the dip angle, and the lowest point of the wave is the dip direction (Donselaar and Schmidt, 2005; Folkestad et al., 2012; Keeton et al., 2015; Lai et al., 2022a).

## 3. Results

### 3.1. Fracture observation and quantitative analysis

Natural fractures are recognized as vertical, high angle, medium angle, low angle and horizontal fractures based on their geometry, and are classified into open, partially open and closed according to their cement filling degree (Zazoun, 2013; Lai et al., 2018). The natural fractures in the deep buried Cretaceous Bashijiqike Formation in the Kuqa depression of Tarim Basin are mainly high angle (>60°) and vertical fractures which are partially to fully cemented by carbonate cements (Fig. 1). The open high angle-vertical fractures can coexist with the cemented fractures (Fig. 1A–G). The fine-medium grained sandstones are more fractured than conglomerates and mudstones (Fig. 1). In addition, some of the early carbonate (calcite) cemented fractures can be dissolved to form vuggy fractures (Fig. 1I–P).

The fractures with an aperture <0.1 mm, which can only be detected by thin sections, are classified as microfractures (Anders et al., 2014). Thin sections and LSCM analysis reveal the microfracture apertures are in the micrometer scales (Fig. 2). The microfractures can occur in the siltstone (Fig. 2A), fine-medium grained sandstones (Fig. 2B–C), and in some cases conglomerates (Fig. 2D–E). Additionally, the microfractures are observed to be partially to fully filled by calcite cements (Fig. 2F–H), and the CL image proves the presence of carbonate cemented fractures (Fig. 2I). LSCM analysis confirms the microfracture with micrometer scale aperture, and the microfracture connects the intergranular and intragranular dissolution pores (Fig. 2J–K).

The CT analysis of the core not only provides 3-D visualization of CT morphology but also can calculate the quantitative fracture parameters, including fracture aperture and porosity (Kyle and Ketcham, 2015; Lai et al., 2017). The hand core measurement shows that there are two open, extensional fractures that generally plunge up-dip (Fig. 3). The fractures appear to be partially open, and the shorter fracture plunges with bedding (Fig. 3). The open fracture appearance (stained cyan) and the calcite cemented fracture (stained magenta) are captured by the scanning images (Fig. 3). Fracture aperture is determined from CT scanning, and the 3-D CT scanning images, and the fracture aperture is mainly

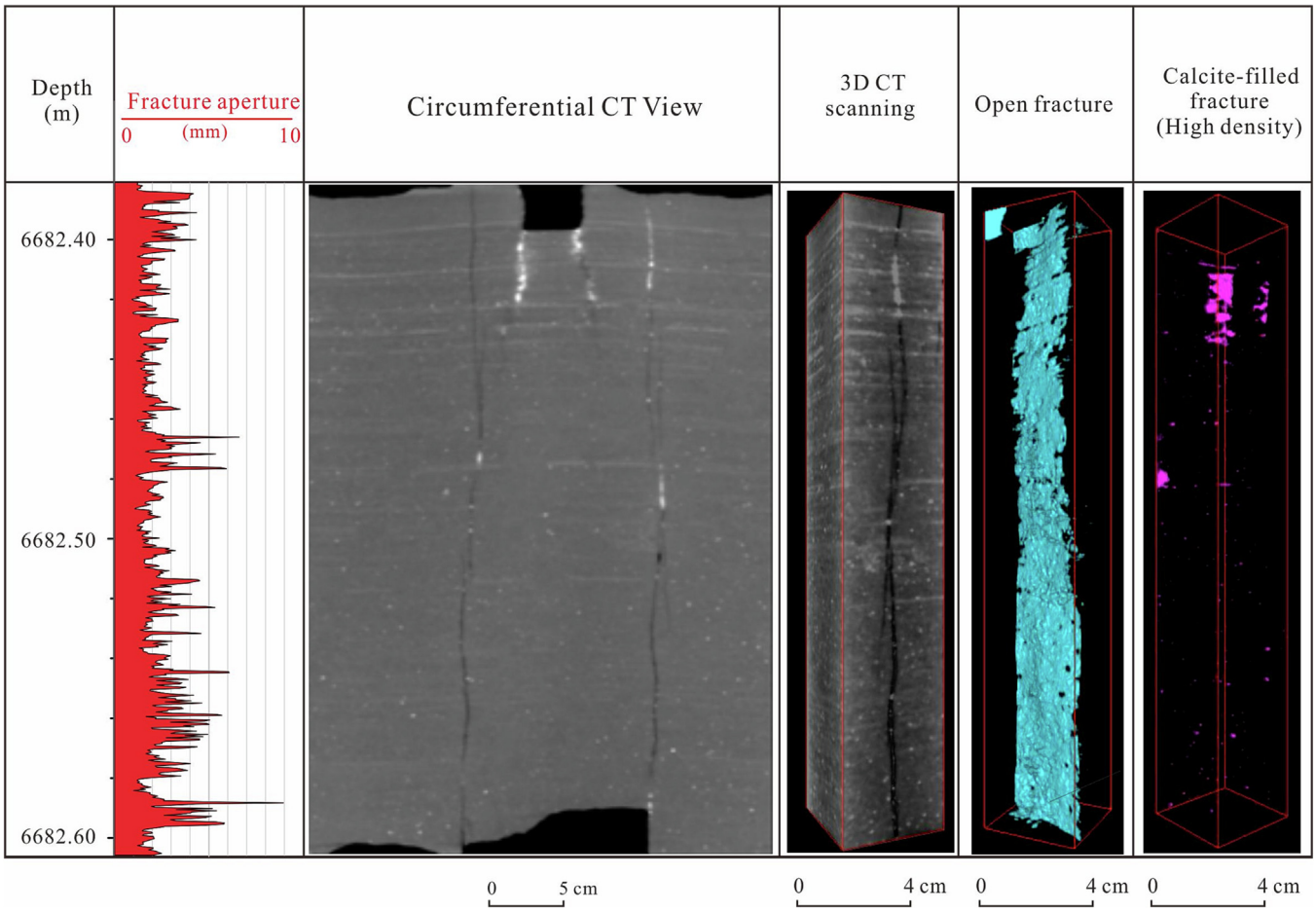


**Fig. 3.** Three-dimensional volume rendering of open fracture and calcite filled fracture (after Lai et al., 2017). The fracture porosity is as high as 4.33%.

in the range from 2 mm to 5 mm (Fig. 3). The fracture porosity is determined as 4.33% by dividing the total fracture volume by the volume of the core segment (Fig. 3). Fracture apertures are sensitivity to stress (Zeng, 2010; Yang et al., 2020). Therefore, fracture porosity derived from laboratory CT analysis is suggested to be higher than the fractures at burial depth (Zeng, 2010; Espinoza et al., 2016; Lai et al., 2017).

### 3.2. In situ stress evaluation

In situ stress directions are easy to be evaluated from image logs since they capture the drilling-induced fractures and borehole breakouts (Prioul et al., 2007; Massiot et al., 2015; Lai et al., 2018). In addition, geophysical well logs can also estimate the in situ stress magnitudes. By calibrating the in-situ stress magnitudes with hydraulic fracturing and acoustic emission method, the following method is proposed to calculate the three mutually orthogonal principal stresses, including vertical stress ($S_v$), minimum horizontal stress ($Sh_{min}$) and maximum horizontal stress ($SH_{max}$) using geophysical well logs (Fig. 4; Zoback et al., 2003; Verweij et al., 2016; Dixit et al., 2017; Lai et al., 2022a; Xu et al., 2022).

$$S_v = \int_0^H \rho g dz \tag{1}$$

$$SH_{max} = \frac{v}{1-v}S_v + \frac{1-2v}{1-v}\alpha P_p + \frac{E}{1-v^2}\varepsilon_H + \frac{Ev}{1-v^2}\varepsilon_h \tag{2}$$

$$Sh_{min} = \frac{v}{1-v}S_v + \frac{1-2v}{1-v}\alpha P_p + \frac{E}{1-v^2}\varepsilon_h + \frac{Ev}{1-v^2}\varepsilon_H \tag{3}$$

In Eqs. (1)–(3), $H$ is the burial depth, m, $\rho$ is the rock bulk density, kg/m$^3$, $g$ is 9.8 m/s$^2$, $P_P$ is pore pressure and can be determined by Eaton's method. $E$ (MPa) is Young's modulus, and $v$ is the Poisson's ratio. $\alpha$ is the Biot's coefficient. The $\varepsilon_H$ and $\varepsilon_h$ are coefficients associated with $SH_{max}$ and $Sh_{min}$ (Lai et al., 2022a; Xu et al., 2022).

The Well D1102 was drilled into an anticline structure which can be evidenced by the seismic profile (Fig. 4). The folded structure, the presence of fractures as well as variations in geomechanical properties (lithology, grain size, beddings) will result in the fluctuations in the in-situ magnitudes (Fig. 4). In isotropic stratigraphy, $Sh_{min}$ will be equal to $SH_{max}$, however, the $SH_{max}$ will be much larger than $Sh_{min}$ in true formation. In addition, the $SH_{max}$ and $Sh_{min}$ difference ($\Delta\sigma = SH_{max} - Sh_{min}$ will vary significantly due to active tectonic activities and the presence of faults and fractures (Fig. 4) (Maleki et al., 2014; Yeltsov et al., 2014; Liu et al., 2017; Ju and Wang, 2018; Lai et al., 2022a).

### 3.3. Image log fracture interpretation

Image logs are specialized tools for subsurface fracture detection (Tokhmchi et al., 2010). Image logs have the advantages of capturing fracture state (open, filled or open-filled), azimuth (dip direction and dip angles) and calculating fracture attributes (porosity and aperture) (Khoshbakht et al., 2009; Kosari et al., 2015; Lai et al., 2018). Cores have revealed the multiple generations of fracturing and mineralization (Fig. 1), and then they are used to calibrate the statically and dynamically normalized image logs to facilitate the recognition of open (conductive) and closed (resistive) fractures (Fig. 1) (Zazoun, 2013; Lai et al., 2023b).

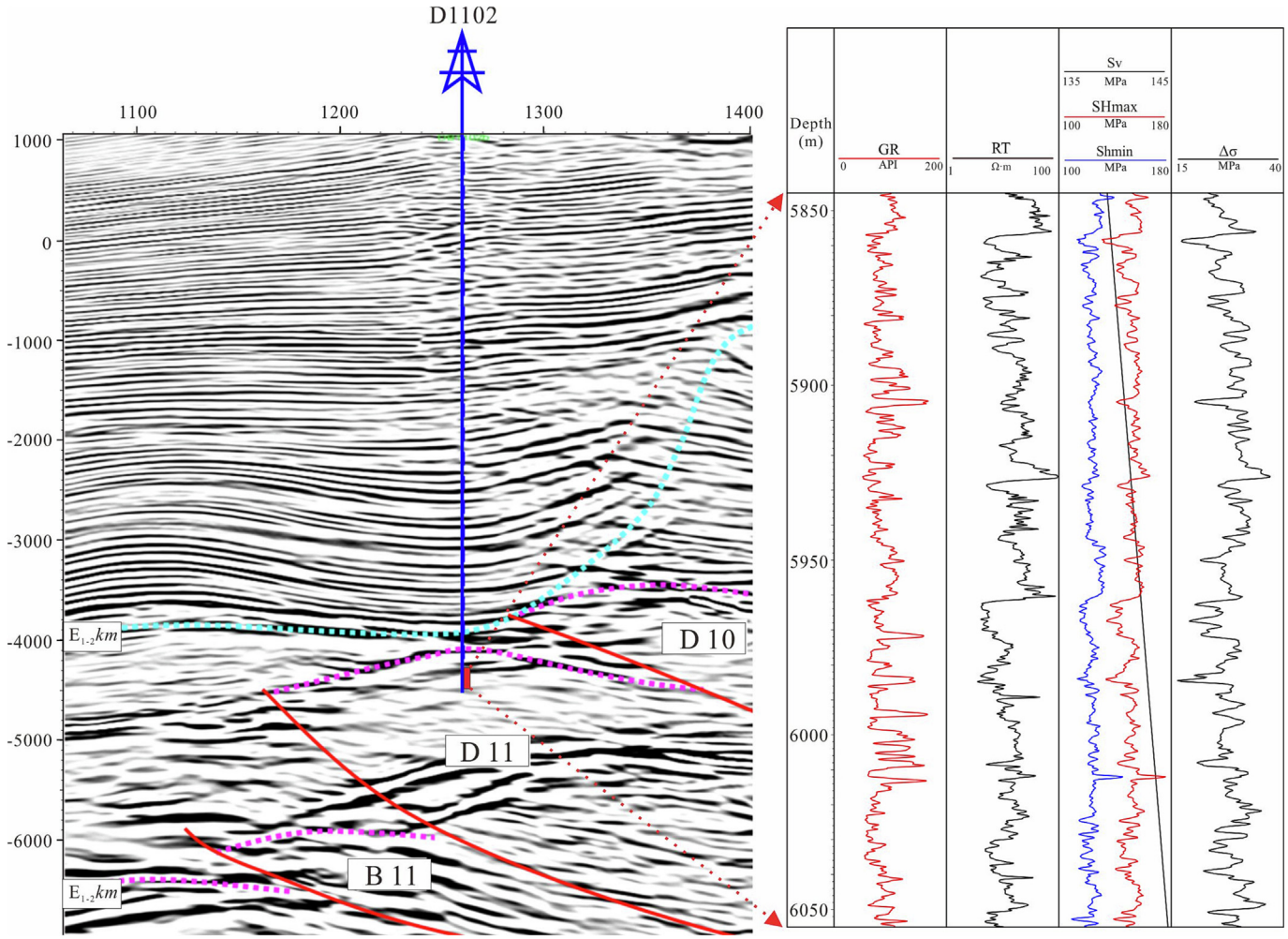


**Fig. 4.** The seismic cross section of Well D1102 drilled into a faulted anticline and the related in situ stress magnitudes.

Image logs trace the dip direction and dip angle of fractures that crosscut the borehole, and there are multiple sets of fractures encountered (Fig. 5). Additionally, in water-based drilling muds, fracture length (FVTL), fracture density (FVDC), fracture porosity (FVPA) as well as fracture aperture (FVA) can be calculated from the electrical image logs (Fig. 5) (Luthi and Souhaite, 1990; Zeng et al., 2013; Xu et al., 2016; Lai et al., 2018). Fracture length is the total fracture length (m) in a unit area of boreholes (1 $m^2$). Fracture (linear) density (FVDC) is the number of fractures per unit length in the direction orthogonal to fracture planes (Prioul et al., 2007; Ameen et al., 2012; Wilson et al., 2015; Lai et al., 2018).

Fracture aperture is the average physical aperture along the trace of the fracture intersection with the borehole and can be estimated by Eq. (4) (Silliman, 1989; Luthi and Souhaite, 1990; Wilson et al., 2015).

$$FVA = aAR_m^b R_{xo}^{1-b} \tag{4}$$

A is the integrated additional current A ($m^2$), $R_{xo}$ and $R_m$ are the resistivities of the invaded zone and drilling muds (Ω·m), $a$ and $b$ are the coefficients related to the imaging tool (Luthi and Souhaite, 1990).

The fracture porosity can be calculated using Eq. (5).

$$FVPA = \frac{1}{2\pi RLC}\sum_{i=1}^{n} L_i W_i \tag{5}$$

$R$ is the borehole radius (m), $L$ is the length of interpretation interval (m), $C$ is the borehole coverage of the imaging tool, $L_i$ is the length of $i^{th}$ fracture (m), and $W_i$ is the $i^{th}$ fracture aperture (Luthi and Souhaite, 1990; Ameen et al., 2012).

The image log fracture interpretation shows that in the 5950 m to 6000 m depth intervals of Well D1102, there are a total of 137 numbers of conductive fractures crosscutting the boreholes, and the linear fracture density is 2.74 $m^{-1}$ (Fig. 5). The average fracture porosity is determined as 0.34%, and the average fracture aperture is 0.63 mm, while the maximum fracture aperture is 5.39 mm (Fig. 5). The maximum fracture porosity can reach as high as 2.67% in the 5978–5979 m depth interval (Fig. 5).

## 4. Discussion

Fracture properties (fracture porosity, aperture) are dependent on fracture diagenesis (mineral precipitation and dissolution) and in situ stress state (direction and magnitudes) (Laubach, 2003; Lai et al., 2019). Though fracture can improve permeability 1–2 orders of magnitude, fracture porosity is generally <0.5% (Zeng and Liu, 2010). Fracture apertures are typically on the order of 10 μm to 2 mm (Nelson, 2001), while fracture density is <0.75 $m^{-1}$, and it may exceed 10 $m^{-1}$ in some cases (Nelson, 2001). In situ stress has a prime control on fracture aperture (and fracture porosity) (Laubach, 2003). Laubach et al. (2004)

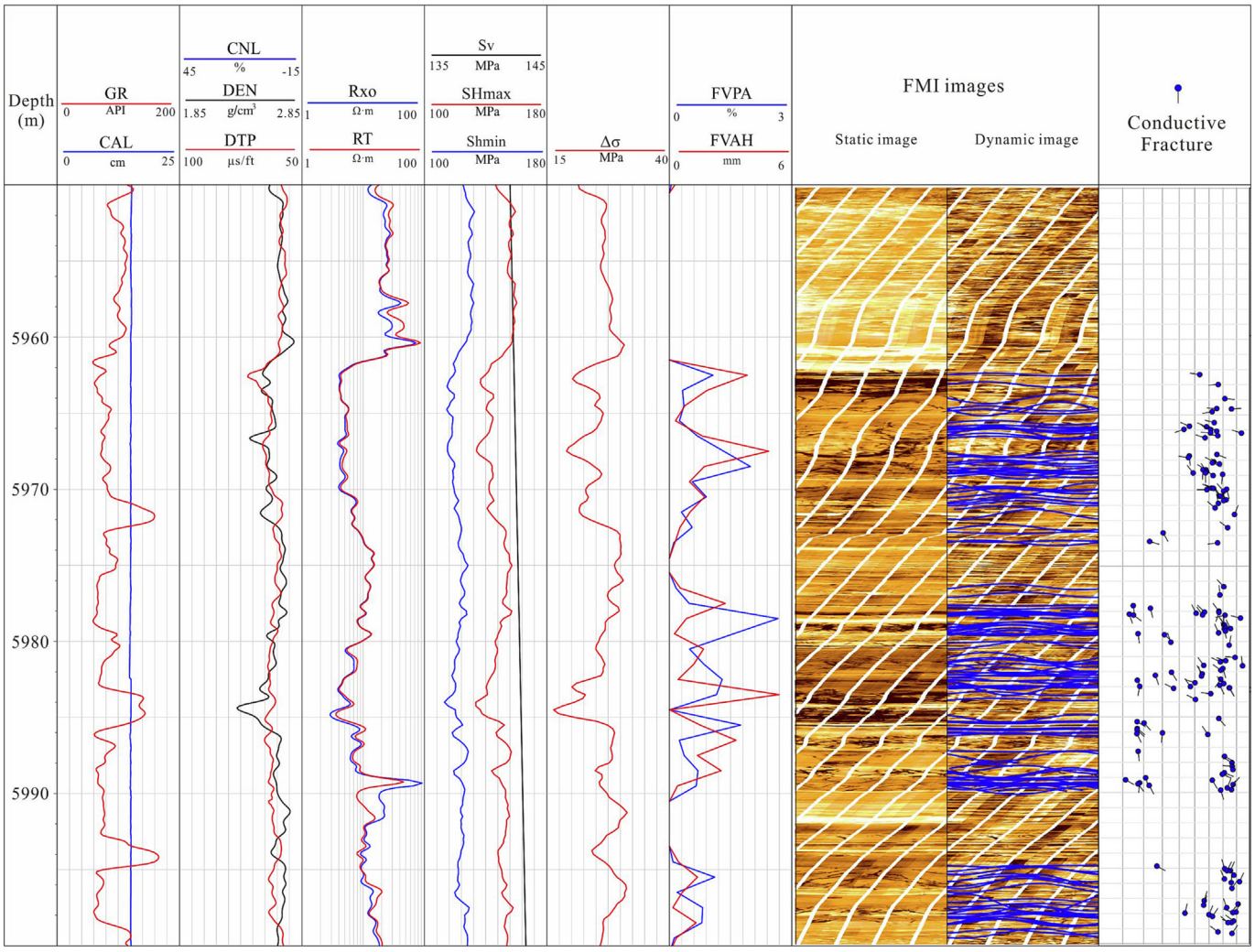


**Fig. 5.** The in situ stress magnitude and fracture porosity and aperture calculated from image logs of Well D1102.

noted that fractures are not necessarily parallel to $SH_{max}$ to keep open status. Therefore in situ stress magnitudes control fracture behaviors. Fracture aperture and fracture porosity will be decreased with the horizontal stress difference (Rajabi et al., 2010; Lai et al., 2019).

There are many complex structures (fold, fault, fault-related fold, etc.) in the Kuqa depression (Lai et al., 2019; Xu et al., 2022), and the complex structural belts will result in varied in situ stress magnitudes (Fig. 4). The high fracture porosity is mainly associated with the low $\Delta\sigma$ (<25 MPa) layers (Fig. 5). High density of fractures is easy to be formed in stress relaxation layers, and the high linear fracture density will result in a high fracture porosity (Fig. 5). In addition, the fractures in the Bashijiqike Formation are mainly high angle fractures. High-angle structural fractures are suggested to keep high apertures than low angle ones. However, the mudstone layers (high GR value intervals) should be excluded even if they have low $\Delta\sigma$ values, since the mudstone intervals commonly lack fractures (Laubach et al., 2009) (Fig. 5). Fractures in this stress state ($\Delta\sigma$ < 25 MPa) are suggested to keep a high fracture aperture and porosity (Fig. 5).

However, there are some fractures having high fracture porosity even with high $\Delta\sigma$ values (Fig. 6). Mineral cementation and dissolution along fracture surfaces have a great impact on fracture properties (Zeng et al., 2013; Laubach et al., 2019; Lai et al., 2022a). Subsurface fractures will improve acids-rich fluid mobility and result in the dissolution along the fracture planes (Matonti et al., 2017; Lai et al., 2022a). Dissolution will result in a rapid opening of the fracture aperture (Starchenko et al., 2016). The vuggy fracture planes (Fig. 1) and the dissolved framework grains along the fracture surfaces (Fig. 2) all indicate a high degree of mineral dissolution (Lai et al., 2022a). The vuggy fractures appear as continuous or discontinuous (conductive, resistive, or mixed) sinusoidal waves on the image logs, indicating the fracture surfaces are evidently enlarged by dissolution (Fig. 6) (Lai et al., 2022a). Intergranular and intragranular dissolution pores are mainly associated with natural fractures, in contrast, there are no evident dissolution pores in samples without fractures (Fig. 2; Lai et al., 2022a). Fracture planes are enlarged by dissolution, and cementation and dissolution can occur simultaneously along fracture surfaces (Lai et al., 2022a).

The fracture density is low when the horizontal stress difference is generally higher than 45 MPa. There are only 5 numbers of fractures detected in the 6820–6822 m depth intervals (Fig. 6). However, the fracture porosity can reach as high as 2.6% at about 6822 m depth of Well K8 (Fig. 6). The maximum fracture aperture is 5.67 mm (Fig. 6). Consequently in the intense in situ stress status ($\Delta\sigma$ > 45 MPa), the dissolution along the fracture surfaces will contribute to the high fracture porosity (>2.0%).

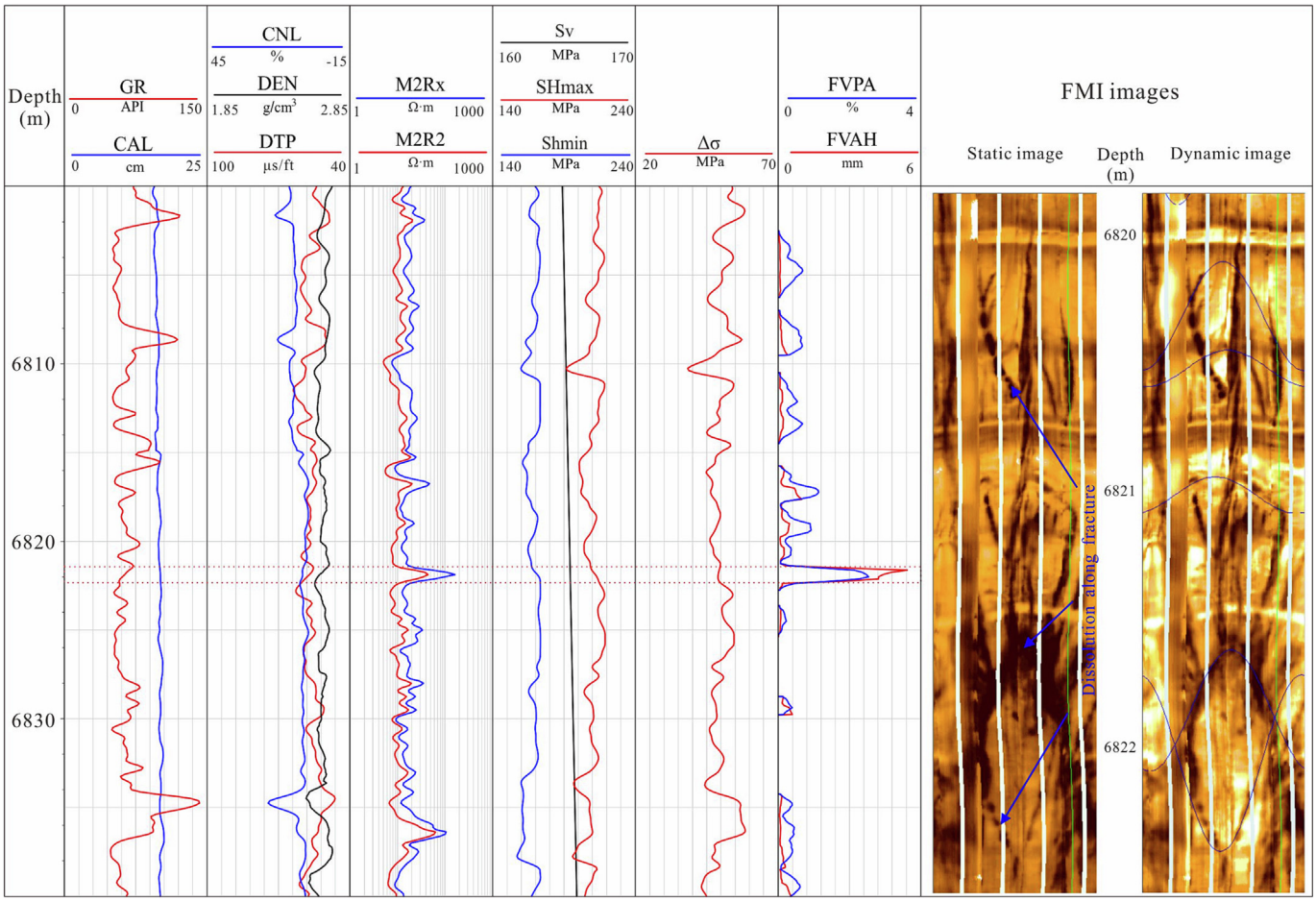


**Fig. 6.** The in situ stress magnitude and fracture porosity and aperture calculated from image logs of Well K8.

## 5. Conclusion

By integrating laboratory observations of fracture porosity with image log-derived fracture porosity at in situ stress conditions, it is found that fracture porosity can keep as high as 2.67%. The low in situ stress magnitudes ($SH_{max}$ and $Sh_{min}$ difference < 25 MPa) and high density of fracture (>2 numbers of fracture per meter) contribute to the high fracture porosity. A high degree of late-stage dissolution along the fracture surfaces enhances fracture aperture and porosity and will result in a high fracture porosity even at high in situ stress magnitudes.

## CRediT authorship contribution statement

**Jin Lai:** Conceptualization, Methodology, Software, Writing – review & editing. **Fei Zhao:** Conceptualization, Methodology, Software. **Mei Zhang:** Data curation, Writing – original draft. **Tianyu Bai:** Data curation, Writing – original draft, Writing – review & editing. **Yuyue Huang:** Visualization, Investigation. **Dong Li:** Visualization, Investigation. **Guiwen Wang:** Conceptualization, Methodology, Software, Validation, Writing – review & editing. **Ziqiang Qin:** Software, Validation, Writing – review & editing.

## Declaration of Competing Interest

The authors declare that they have no known competing financial interests or personal relationships that could have appeared to influence the work reported in this paper.

## Acknowledgments

This work is financially supported by National Natural Science Foundation of China (Grant No. 42002133), Strategic Cooperation Project of PetroChina and China University of Petroleum, Beijing (CUPB) (Grant No. ZLZX2020-01-05) and Science Foundation of CUPB (Grant No. 2462021YXZZ003). The authors thank PetroChina Tarim Company for their data assistance.

## References

Ameen, M.S., MacPherson, K., Al-Marhoon, M.I., Rahim, Z., 2012. Diverse fracture properties and their impact on performance in conventional and tight-gas reservoirs, Saudi Arabia: The Unayzah, South Haradh case study. AAPG Bull. 96 (3), 459–492.

Anders, M.H., Laubach, S.E., Scholz, C.H., 2014. Microfractures: a review. J. Struct. Geol. 69, 377–394.

Brekke, H., MacEachern, J.A., Roenitz, T., Dashtgard, S.E., 2017. The use of microresistivity image logs for facies interpretations: an example in point-bar deposits of the McMurray Formation, Alberta, Canada. AAPG Bull. 101 (5), 655–682.

Chandra, D., Vishal, V., 2021. A critical review on pore to continuum scale imaging techniques for enhanced shale gas recovery. Earth Sci. Rev. 217, 103638.

Dixit, N.C., Hanks, C.L., Wallace, W.K., Ahmadi, M., Awoleke, O., 2017. In situ stress variations associated with regional changes in tectonic setting, northeastern Brooks Range and eastern North Slope of Alaska. AAPG Bull. 101 (3), 343–360.

Donselaar, M.E., Schmidt, J.M., 2005. Integration of outcrop and borehole image logs for high-resolution facies interpretation: example from a fluvial fan in the Ebro Basin, Spain. Sedimentology 52, 1021–1042. https://doi.org/10.1111/j.1365-3091.2005.00737.x.

Espinoza, D.N., Shovkun, I., Makni, O., Lenoir, N., 2016. Natural and induced fractures in coal cores imaged through X-ray computed microtomography-impact on desorption time. Int. J. Coal Geol. 154–155, 165–175.

Folkestad, A., Veselovsky, Z., Roberts, P., 2012. Utilising borehole image logs to interpret delta to estuarine system: a case study of the subsurface Lower Jurassic Cook Formation in the Norwegian northern North Sea. Mar. Pet. Geol. 29, 255–275.
Hyman, J.D., Sweeney, M.R., Frash, L.P., Carey, J.W., Viswanathan, H.S., 2021. Scale-bridging in three dimensional fracture networks: characterizing the effects of variable fracture apertures on network-scale flow channelization. Geophys. Res. Lett. 48.
Ju, W., Wang, K., 2018. A preliminary study of the present-day in-situ stress state in the Ahe tight gas reservoir, Dibei Gasfield, Kuqa Depression. Mar. Pet. Geol. 96, 154–165.
Keeton, G., Pranter, M., Cole, R.D., Gustason, E.R., 2015. Stratigraphic architecture of fluvial deposits from borehole images, spectral-gamma-ray response, and outcrop analogs, Piceance Basin, Colorado. AAPG Bull. 99 (10), 1929–1956.
Khoshbakht, F., Memarian, H., Mohammadnia, M., 2009. Comparison of Asmari, Pabdeh and Gurpi formation's fractures, derived from image log. J. Pet. Sci. Eng. 67, 65–74.
Kosari, E., Ghareh-Cheloo, S., Kadkhodaie-Ilkhchi, A., Bahroudi, A., 2015. Fracture characterization by fusion of geophysical and geomechanical data: a case study from the Asmari reservoir, the Central Zagros fold-thrust belt. J. Geophys. Eng. 12, 130–143.
Kyle, J.R., Ketcham, R.A., 2015. Application of high resolution X-ray computed tomography to mineral deposit origin, evaluation, and processing. Ore Geol. Rev. 65, 821–839.
Lai, J., Wang, G., Fan, Z., Chen, J., Qin, Z., Xiao, C., Wang, S., Fan, X., 2017. Three-dimensional quantitative fracture analysis of tight gas sandstones using industrial computed tomography. Sci. Rep. 7, 1825.
Lai, J., Wang, G., Fan, Q., Pang, X., Li, H., Zhao, F., Li, Y., Zhao, X., Zhao, Y., Huang, Y., Bao, M., Qin, Z., Wang, Q., 2022b. Geophysical well log evaluation in the era of unconventional hydrocarbon resources: A review on current status and prospects. Surveys in Geophysics 43, 913–957.
Lai, J., Wang, G., Fan, Q., Zhao, F., Zhao, X., Li, Y., Zhao, Y., Pang, X., 2023a. Towards the scientific interpretation of geophysical well logs: typical misunderstandings and countermeasures. Surveys in Geophysics 44, 463–494.
Lai, J., Li, D., Bai, T.Y., Zhao, F., Ai, Y., Liu, H.K., Cai, D.Y., Wang, G.W., Chen, K.J., 2023b. Reservoir quality evaluation and prediction in ultra-deep tight sandstones in the Kuqa depression, China. Journal of Structural Geology 170, 104850.
Lai, J., Wang, G., Wang, S., Cao, J., Li, M., Pang, X., Han, C., Fan, X., Yang, L., He, Z., Qin, Z., 2018. A review on the applications of image logs in structural analysis and sedimentary characterization. Mar. Pet. Geol. 95, 139–166.
Lai, J., Li, D., Ai, Y., Liu, H., Cai, D., Chen, K., Xie, Y., Wang, G., 2022a. Structural diagenesis in ultra-deep tight sandstones in Kuqa depression, Tarim Basin, China. Solid Earth 13, 975–1002.
Lai, J., Li, D., Wang, G., Xiao, C., Hao, X., Luo, Q., Lai, L., Qin, Z., 2019. Earth stress and reservoir quality evaluation in high and steep structure: the Lower Cretaceous in the Kuqa Depression, Tarim Basin, China. Mar. Pet. Geol. 101, 43–54.
Lai, J., Wang, S., Zhang, C., Wang, G., Song, Q., Chen, X., Yang, K., Yuan, C., 2020. Spectrum of pore types and networks in the deep Cambrian to Lower Ordovician dolostones in Tarim Basin, China. Mar. Petrol. Geol. 112, 104081.
Lai, J., Liu, S., Xin, Y., Wang, S., Xiao, C., Song, Q., Chen, X., Wang, G., Qin, Z., Ding, X., 2021. Geological-petrophysical insights in the deep Cambrian dolostone reservoirs in Tarim Basin, China. AAPG Bull. 105 (11), 2263–2296.
Laubach, S.E., 2003. Practical approaches to identifying sealed and open fractures. AAPG Bull. 87 (4), 561–579.
Laubach, S.E., Olson, J.E., Gale, J.F.W., 2004. Are open fractures necessarily aligned with maximum horizontal stress? Earth Planet. Sci. Lett. 222 (1), 191–195.
Laubach, S.E., Olson, J.E., Gross, M.R., 2009. Mechanical and fracture stratigraphy. AAPG Bull. 93 (11), 1413–1426.
Laubach, S.E., Lander, R.H., Criscenti, L.J., Anovitz, L.M., Urai, J.L., Pollyea, R.M., Hooker, J.N., Narr, W., Evans, M.A., Kerisit, S.N., Olson, J.E., Dewers, T., Fisher, D., Bodnar, R., Evans, B., Dove, P., Bonnell, L.M., Marder, M.P., Pyrak-Nolte, L., 2019. The role of chemistry in fracture pattern development and opportunities to advance interpretations of geological materials. Rev. Geophys. 57 (3), 1065–1111.
Liu, J., Ding, W., Yang, H., Wang, R., Yin, S., Li, A., Fu, F., 2017. 3D geomechanical modeling and numerical simulation of in-situ stress fields in shale reservoirs: a case study of the lower Cambrian Niutitang formation in the Cen'gong block, South China. Tectonophysics 712–713, 663–683.
Luthi, S., Souhaite, P., 1990. Fracture apertures from electrical borehole scans. Geophysics 55 (7), 821–833.
Maleki, S., Moradzadeh, A., Riabi, R.G., Sadaghzadeh, F., 2014. Comparison of several different methods of in situ stress determination. Int. J. Rock Mech. Min. Sci. 71 (71), 395–404.
Massiot, C., Mcnamara, D.D., Lewis, B., 2015. Processing and analysis of high temperature geothermal acoustic borehole image logs in the Taupo volcanic zone, New Zealand. Geothermics 53, 190–201.
Massiot, C.J., Nicol, T.A., McNamara, D.D., 2017. Statistical methods of fracture characterization using acoustic borehole televiewer log interpretation. J. Geophys. Res. Solid Earth 122, 6836–6852.
Matonti, C., Guglielmi, Y., Viseur, S., Garambois, S., Marié, L., 2017. P-wave velocity anisotropy related to sealed fractures reactivation tracing the structural diagenesis in carbonates. Tectonophysics 705, 80–92.
Movahed, Z., Junin, R., Safarkhanlou, Z., Akbar, M., 2014. Formation evaluation in Dezful embayment of Iran using oil-based-mud imaging techniques. J. Pet. Sci. Eng. 121, 23–37.
Nelson, R., 2001. Geologic analysis of naturally fractured reservoirs. Gulf Professional Publishing, pp. 96–104.
Pengda, C., Shen Weijun, X.u., Xiaobing, Q.L., Chao, Q., Yue, C., 2022. Multiphysics coupling study of near-wellbore and reservoir models in ultra-deep natural gas reservoirs. J. Pet. Explor. Prod. Technol. 12, 2203–2212.
Prioul, R., Donald, A., Koepsell, R., Marzouki, Z.E., Bratton, T., 2007. Forward modeling of fracture-induced sonic anisotropy using a combination of borehole image and sonic logs. Geophysics 72 (4), 135–147.
Rajabi, M., Sherkati, S., Bohloli, B., Tingay, M., 2010. Subsurface fracture analysis and determination of in-situ stress direction using FMI logs: an example from the Santonian carbonates (Ilam Formation) in the Abadan Plain, Iran. Tectonophysics 492, 192–200.
Shen, W., Ma, T., Li, X., Sun, B., Hu, Y., Xu, J., 2022. Fully coupled modeling of two-phase fluid flow and geomechanics in ultra-deep natural gas reservoirs. Phys. Fluids 34, 043101.
Silliman, S., 1989. An interpretation of the difference between aperture estimates derived from hydraulic and tracer tests in a single fracture. Water Resour. Res. 25 (10), 2275–2283.
Spooner, V.E., Geiger, S., Arnold, D., 2021. Dual-porosity flow diagnostics for spontaneous imbibition in naturally fractured reservoirs. Water Resour. Res. 57, e2020WR02777.
Starchenko, V., Marra, C.J., Ladd, A.J.C., 2016. Three-dimensional simulations of fracture dissolution. J. Geophys. Res. Solid Earth 121, 6421–6444.
Tokhmchi, B., Memarian, H., Rezaee, M.R., 2010. Estimation of the fracture density in fractured zones using petrophysical logs. J. Pet. Sci. Eng. 72, 206–213.
Verweij, J.M., Boxem, T.A.P., Nelskamp, S., 2016. 3D spatial variation in vertical stress in on- and offshore Netherlands; integration of density log measurements and basin modeling results. Mar. Pet. Geol. 78, 870–882.
Wilson, M.E.J., Lewis, D., Yogi, O., Holland, D., Hombo, L., Goldberg, A., 2013. Development of a Papua New Guinean onshore carbonate reservoir: a comparative borehole image (BHI) and petrographic evaluation. Mar. Pet. Geol. 44, 164–195.
Wilson, T.H., Smith, V., Brown, A., 2015. Developing a model discrete fracture network, drilling, and enhanced oil recovery strategy in an unconventional naturally fractured reservoir using integrated field, image log, and three-dimensional seismic data. AAPG Bull. 99 (4), 735–762.
Xu, K., Yang, H., Zhang, H., Ju, W., Li, C., Fang, L., Wang, Z., Wang, H., Yuan, F., Zhao, B., Zhang, W., Liang, J., 2022. Fracture effectiveness evaluation in ultra-deep reservoirs based on geomechanical method, Kuqa Depression, Tarim Basin, NW China. J. Pet. Sci. Eng. 215, 110604.
Xu, J., Zhang, B., Qin, Y., Cao, G., Zhang, H., 2016. Method for calculating the fracture porosity of tight-fracture reservoirs. Geophysics 81 (4), IM57-IM70.
Yang, Y., Tao, L., Yang, H., Iglauer, S., Wang, X., Askari, R., Yao, J., Zhang, K., Zhang, L., Sun, H., 2020. Stress sensitivity of fractured and vuggy carbonate: an X-ray computed tomography analysis. J. Geophys. Res.: Solid Earth 125, e2019JB01875.
Yeltsov, I.N., Nazarova, L.A., Nazarov, L.A., Nesterova, G.V., Sobolev, A.Y., Epov, M.I., 2014. Geomechanics and fluid flow effects on electric well logs: multiphysics modeling. Russ. Geol. Geophys. 55 (5–6), 775–783.
Zazoun, R.S., 2013. Fracture density estimation from core and conventional well logs data using artificial neural networks: the Cambro-Ordovician reservoir of Mesdar oil field, Algeria. J. Afr. Earth Sc. 83, 55–73.
Zeng, L., 2010. Microfracturing in the Upper Triassic Sichuan Basin tight-gas sandstones: tectonic, overpressure, and diagenetic origins. AAPG Bull. 94 (12), 1811–1825.
Zeng, L., Liu, H., 2010. Influence of fractures on the development of low-permeability sandstone reservoirs: a case study from the Taizhao district, Daqing Oilfield, China. J. Pet. Sci. Eng. 72, 120–127.
Zeng, L., Su, H., Tang, X., Peng, Y., Gong, L., 2013. Fractured tight sandstone oil and gas reservoirs: a new play type in the Dongpu depression, Bohai Bay Basin, China. AAPG Bull. 97 (3), 363–377.
Zhang, Y., Yang, S., Zhang, Z., Li, Q., Deng, H., Chen, J., Geng, W., Wang, M., Chen, Z., Chen, H., 2022. Multiscale pore structure characterization of an ultra-deep carbonate gas reservoir. J. Pet. Sci. Eng. 208, 109751.
Zoback, M., Barton, C., Brudy, M., Castillo, D., Finkbeiner, T., Grollimund, B., Moos, D., Peska, P., Ward, C., Wiprut, D., 2003. Determination of stress orientation and magnitude in deep wells. Int. J. Rock Mech. Min. Sci. 40, 1049–1076.